Available online at www.sciencedirect.com
ScienceDirect
Materials Research Bulletin 42 (2007) 2192–2201
Materials Research Bulletin
www.elsevier.com/locate/matresbu

Plasmon–phonon and plasmon–two different phonon interaction in $Pb_{1-x}Mn_xTe$ mixed crystals

J. Trajić [a], N. Romčević [a,*], M. Romčević [a], V.N. Nikiforov [b]

[a] *Institute of Physics, P.O. Box 68, 11080 Belgrade, Serbia and Montenegro*
[b] *Low-Temperature Physics Department, Moscow State University, 119899 Moscow, Russia*

Received 16 November 2006; accepted 5 January 2007
Available online 11 January 2007

Abstract

Far-infrared reflection spectra in wide temperature range was used to investigate the vibrational properties of $Pb_{1-x}Mn_xTe$ ($x = 0.0002$, 0.002, 0.02 and 0.1) mixed crystals. To analyse the experimental results we use dielectric function that takes into account the existence of plasmon–phonon as well as the plasmon–two different phonon interaction. The best fit method revealed two frequencies of plasmon–phonon coupled modes and three frequencies of plasmon–two different phonon coupled modes. Further, the values for two different LO modes and plasma frequency (ω_P) are calculated. Results obtained from experimental spectra as the best fit, are in very good agreement with the theoretical prediction. The model of phonon behaviour based on Genzel's model was developed. It was found that the long wavelength optical phonon modes of these mixed crystals, exhibit an intermediate and two mode behaviour, coincidentally.

Keywords: A. Semiconductors; C. Infrared spectroscopy; D. Optical properties

1. Introduction

The lead–telluride family of the IV–VI compounds are narrow-gap semiconductors. Depending on composition their band gap can vary from almost 0 to 0.3 eV [1–5]. The lead–telluride and its solid solutions are used for active and passive devices. Namely, it is well known [3], that in lead chalcogenides electrical active native point defect (vacancies and interstitial atoms) produce energy states lying either above the bottom of the conduction band (donor defects) or bellow the top of valence band (acceptors). This leads to high charge carrier concentration in undoped crystals because of the deviation of composition from stoichiometry. Furthermore, neither cooling nor magnetic field has been observed to have the freeze-out effect on charge carriers.

Solid solution $Pb_{1-x}Mn_xTe$ is semimagnetic semiconductor that is not sufficiently studied [6–9]. Their crystal structure is cubic (NaCl-type), the lattice parameter change linearly while the manganese concentration vary.

If the manganese concentration is less than 20 at.%, Mn enters the PbTe lattice as Mn^{2+}, and is not the electroactive dopant. Doping of PbTe with Mn increases the band gap at the rate $\partial E_g/\partial x \cong (38–48)$ meV/% MnTe [10], but does not provide appearance of local or quasilocal level in the vicinity of the actual bands [7].

* Corresponding author. Tel.: +381 11 3160 346; fax: +381 11 3160 531.
E-mail address: romcevi@phy.bg.ac.yu (N. Romčević).

0025-5408/$ – see front matter © 2007 Elsevier Ltd. All rights reserved.
doi:10.1016/j.materresbull.2007.01.003

MnTe itself is very interesting material. Namely, all manganese-chalcogenides are antiferromagnetic insulators [11–14], having NaCl type of crystal structure. MnTe differs from the other manganese-chalcogenides (MnO, MnS and MnSe), as it has stable orthorhombic NiAs type of crystal structure, as well as stable high-temperature cubic NaCl type structure [15].

In this paper, we present results obtained by using far infrared spectroscopy (FIR) to study optical properties of the $Pb_{1-x}Mn_xTe$ mixed crystals. Analysis of reflection spectra carried out in wide spectral range shows that in that system the plasmon–phonon and plasmon–two different phonon coupling exists both at the same time.

2. Samples and experiment

The synthesis procedure for the preparation of the single crystals of $Pb_{1-x}Mn_xTe$ has been already described in our previous papers [16–18]. Briefly, single crystals of $Pb_{1-x}Mn_xTe$ were grown by the modified Bridgman method with a lowering rate of 1 mm/h. The sample was produced by synthesis from the high purity elements. The chemical composition of the samples was checked by an electron microprobe, which revealed good chemical homogeneity of the material.

The specimens were cut parallel to (1 0 0) (the cleaving plane), with an inner blade diamond cutter and then mechanically polished.

The widely known etch pit technique is very suitable for studies of the crystalline solids. For such studies, cleavage planes are often preferred to the mature surface because the former are free from the usual growth features and the characteristic surface marking which affects each of the patterns produced. Microscopic observation of the chemically etched (1 0 0) surfaces also revealed other structural characteristic. It was confirmed that $Pb_{1-x}Mn_xTe$ single crystals and low-angle grain boundary free crystals were obtained in cases of $x = 0.0002$, 0.002 and 0.02. In the case of 10% Mn ($x = 0.1$), polycrystalline material was obtained. Also, neither cellular structure nor metal inclusions were observed.

The chemical composition of $Pb_{1-x}Mn_xTe$ crystals were determined by the XRD technique [16,17]. All the samples were examined under the same conditions, using the Philips PW 1729 X-ray generator, the Philips 1710 diffractometer and the original APD software.

In our paper [17] we presented X-ray diffractogram of powdered $Pb_{1-x}Mn_xTe$. We find out that excluding reflection which corresponds to PbTe, small reflections belonging to MnTe are present, coming from Mn which occurs in two different cells: orthorhombic and cubic. In the case of $Pb_{0.98}Mn_{0.02}Te$, except reflection which corresponds to PbTe, we registered four small reflections at $2\theta = 21.8^\circ$, 28.26°, 43.88° and 62.88°. The first two belong to MnTe which has cubic crystal structure corresponding to planes (1 1 1) and (2 1 0) [19], while the other two correspond to planes (1 2 1) and (3 2 1) when MnTe has orthorhombic structure [20]. X-ray diffractogram of $Pb_{0.9}Mn_{0.1}Te$, except PbTe reflections shows two more reflections, one from (1 1 1) plane, which belong to cubic MnTe [19] and second from plane (3 2 1), from orthorhombic MnTe [20]. Our calculated results for the lattice parameters of $Pb_{1-x}Mn_xTe$ show that samples with $x \leq 0.02$ obey to Vegards rule, meaning that lattice constant as function of a manganese mole fraction (x) is: $a(x) = (0.6462 \pm 0.0632x)$ nm, which is in good agreement with literature values [3].

3. Reflectivity analysis and fitting procedure

The theoretical model for the bulk dielectric function has been discussed by several authors [21,22]. We note briefly that the low-frequency dielectric properties of PbTe and related compounds have been described with not less than two classical oscillators ($l \geq 2$) corresponding to the TO-modes, superimposed by a Drude part that takes into account the free carrier contribution [23]:

$$\varepsilon_S(\omega) = \varepsilon_\infty + \sum_{k=1}^{l} \frac{\varepsilon_\infty(\omega_{LOk}^2 - \omega_{TOk}^2)}{\omega_{TOk}^2 - \omega^2 - i\gamma_{TOk}\omega} - \frac{\varepsilon_\infty \omega_P^2}{\omega(\omega + i\gamma_P)} \quad (1)$$

where ε_∞ is the bound charge contribution and is considered as a constant, ω_{LOk} and ω_{TOk} the longitudinal and transverse optical-phonon frequencies, ω_P the plasma frequency, and γ_{TOk} and γ_P the phonon and plasma damping. In the PbTe-based systems the pure LO-modes ($\omega_{LO,PbTe}$) of the lattice are strongly influenced by the plasmon mode (ω_P) of free carriers. As a result a combined plasmon–LO phonon modes ($\omega_\pm$) were observed [24]. In the experimental

spectra only coupled mode positions are observable. Therefore the LO-mode could be determined only if the influence of the free carrier contraction will be eliminated [25]. Heaving this in mind, in the analysis of reflectivity spectra of $Pb_{1-x}Mn_xTe$ we have decided to use dielectric function which takes into account the existence of plasmon–LO phonon interaction in advance [25]:

$$\varepsilon(\omega) = \varepsilon_\infty \frac{\prod_{j=1}^{m+n}(\omega^2 + i\gamma_{lj}\omega - \omega_{lj}^2)}{\omega^m \prod_{i=1}^{m}(\omega + i\gamma_{Pi}) \prod_{i=1}^{n}(\omega^2 + i\gamma_{ti}\omega - \omega_{ti}^2)} \prod_{k=1}^{s} \frac{\omega^2 + i\gamma_{kLO} - \omega_{kLO}^2}{\omega^2 + i\gamma_{kTO} - \omega_{kTO}^2} \tag{2}$$

The first term in Eq. (2) represents coupling of m plasmons and n phonons, while the second term represents uncoupled modes of the crystal(s), while $l = n + s$. The ω_{lj} and γ_{lj} parameters of the first numerator are eigenfrequencies and damping coefficients of the longitudinal plasmon–n phonon waves. The parameters of the first denominator correspond to the similar characteristics of the transverse (TO) vibrations. In the second term ω_{LO} and ω_{TO} are the longitudinal and transverse frequencies, while γ_{LO} and γ_{TO} are damping. In the case of plasmon–LO phonon coupling $m = 1$ and $n = 1$.

The case, which considers coupling of one plasmon and one phonon, is explained in detail in Ref. [25]. The coupled mode positions are defined as the solutions of a real part of Eq. (1) ($\mathrm{Re}\{\varepsilon_S\} = 0$), and they are given by:

$$2\omega_\pm^2 = \omega_{LO}^2 + \omega_P^2 \pm \sqrt{(\omega_{LO}^2 + \omega_P^2)^2 - 4\omega_P^2\omega_{TO}^2} \tag{3}$$

On that way, in principle, its $\omega_{lj} = \omega_\pm$ ($j = 1, 2$). The values of coupled plasmon–phonon modes were determined using fitting procedure, while the values of initial $\omega_{LO,PbTe}$ and ω_P modes are determined by using the following equations:

$$\omega_P = \frac{\omega_{l1}\omega_{l2}}{\omega_t}, \qquad \omega_{LO,PbTe}^2 = \omega_{l2}^2 - \omega_P^2\left[1 - \left(\frac{\omega_t}{\omega_{l2}}\right)^2\right] \tag{4}$$

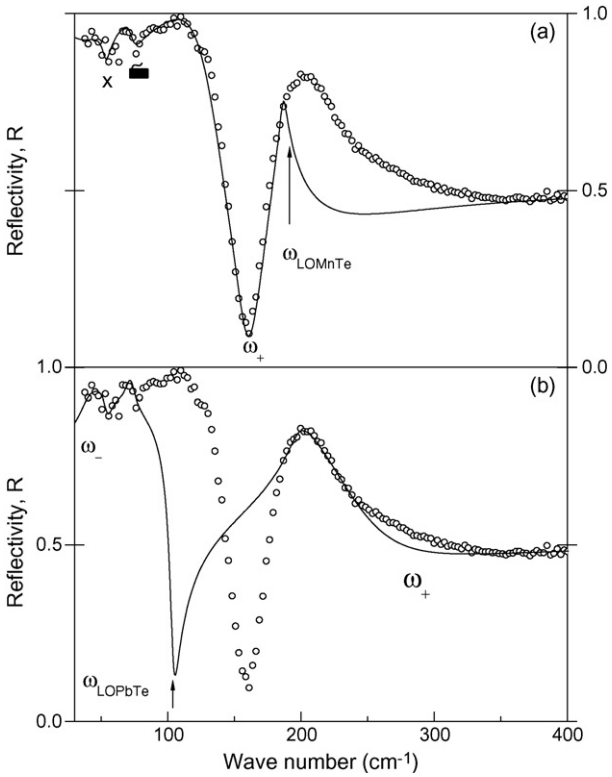

Fig. 1. Far-infrared reflection spectrum of the $Pb_{0.98}Mn_{0.02}Te$ at temperature of 80 K. Experimental data are represented by circle, while solid line is calculated spectrum obtained by a fitting procedure based on the model for plasmon–phonon coupling (Eq. (2); $m = 1$ and $n = 1$), with two sets of parameters.

The far-infrared reflection spectrum of the $Pb_{0.98}Mn_{0.02}Te$ at temperature of 80 K is presented in Fig. 1. Experimental data are presented by circles, while solid line is calculated spectra obtained by a fitting procedure based on the model for plasmon–phonon coupling. The $Pb_{1-x}Mn_xTe$ solid solution phonon structure constitutes of two TO/LO phonon pairs, which originate from starting components PbTe and MnTe. Phonon position changing depending on alloy composition is described in Section 4. According to the suggested plasmon–phonon interaction model it is obvious that only one LO phonon interacts with plasma. Another phonon position is unchangeable.

Based on assumptions that PbTe origin TO/LO pair interacts with plasma (Fig. 1a) and MnTe origin TO/LO pair does not, we get good overlapping of experimental and theoretical spectra only in interaction range. The similar situation is in case when MnTe origin TO/LO pair interacts, too (Fig. 1b). Phonon, properties of which are discussed in detail in Section 4, is denoted with x in both cases. Mod at about 73 cm^{-1}, denoted with $\triangle$, is well known PbTe Brioulene zone edge mode [17].

Consequently, we have decided use dielectric function which takes into account the existence of plasmon–two different LO phonon interaction in the analysis of the reflectivity spectra of $Pb_{1-x}Mn_xTe$. That corresponds to $l = 2$ in dielectric function given by Eq. (1). As we already observed the coupled mode positions are defined as the solutions of the real part of Eq. (1) ($\mathrm{Re}\{\varepsilon_S\} = 0$). In this case, there are three coupled modes, which can be calculated by solving the equations:

$$\omega^6 - A\omega^4 - B\omega^2 - C = 0 \tag{5}$$

where:

$$A = \omega_{LO1}^2 + \omega_{LO2}^2 + \omega_P^2 \tag{6}$$

$$B = \omega_{LO1}^2 \cdot \omega_{LO2}^2 + \omega_P^2(\omega_{TO1}^2 + \omega_{TO2}^2) \tag{7}$$

$$C = \omega_{TO1}^2 \cdot \omega_{TO2}^2 \cdot \omega_P^2 \tag{8}$$

If we use the dielectric function defined by Eq. (2), the values of initial ω_{LO1}, ω_{LO2} (which are two different phonons) and ω_P modes can be determined by:

$$\omega_P = \frac{\omega_{l1}\omega_{l2}\omega_{l3}}{\omega_{t1}\omega_{t2}} \tag{9}$$

$$\omega_{LO1,2}^2 = \frac{1}{2}(\omega_{l1}^2 + \omega_{l2}^2 + \omega_{l3}^2 - \omega_P^2) \pm \sqrt{\left(\frac{1}{4}(\omega_{l1}^2 + \omega_{l2}^2 + \omega_{l3}^2 - \omega_P^2)^2 - \omega_{l1}^2 \cdot \omega_{l2}^2 - \omega_{l2}^2 \cdot \omega_{l3}^2 - \omega_{l1}^2 \cdot \omega_{l3}^2 + \omega_P^2(\omega_{t1}^2 + \omega_{t2}^2)\right)} \tag{10}$$

The far-infrared reflection spectrum of the $Pb_{0.98}Mn_{0.02}Te$ at temperature of 80 K is presented in Fig. 2. Solid line is calculated spectra obtained by a fitting procedure based on the model for plasmon–two different phonon coupling ($m = 1$, $n = 2$ in Eq. (2)). As one can see from the figure, plasmon–two different phonon coupling model, agrees well with the experimental curve for frequencies larger then 190 cm^{-1}, but it is diverges from the experimental results at lower frequencies (Fig. 2a). It is possible to select set of parameters that result in good overlapping in ω_{l2} frequency range, but difference in spectra above 190 cm^{-1} occurs in that case (Fig. 2b). We did not succeed to determinate set of parameters that provide good spectra overlapping in whole range and correspond to the parameters calculated from the model (described in Section 4) at the same time. It is important to point out that the theoretical model [26] is accepted and well known already 30 years and use for verification of parameters determined by fitting procedure. Thus we used dielectric function which in advance takes into account existance of both plasmon–LO phonon and plasmon–two different LO phonon coupling to analyze reflection spectra of solid solution $Pb_{1-x}Mn_xTe$:

$$\varepsilon(\omega) = \varepsilon_\infty \frac{\prod_{j=1}^{2}(\omega^2 + i\gamma_{Lj}\omega - \omega_{Lj}^2)}{\omega(\omega + i\gamma_P)(\omega^2 + i\gamma_t\omega - \omega_t^2)} \frac{\prod_{j=1}^{3}(\omega^2 + i\gamma_{lj}\omega - \omega_{lj}^2)}{\omega(\omega + i\gamma_P)\prod_{j=1}^{2}(\omega^2 + i\gamma_{tj}\omega - \omega_{tj}^2)} \prod_{k=1}^{s} \frac{\omega^2 + i\gamma_{kLO} - \omega_{kLO}^2}{\omega^2 + i\gamma_{kTO} - \omega_{kTO}^2} \tag{11}$$

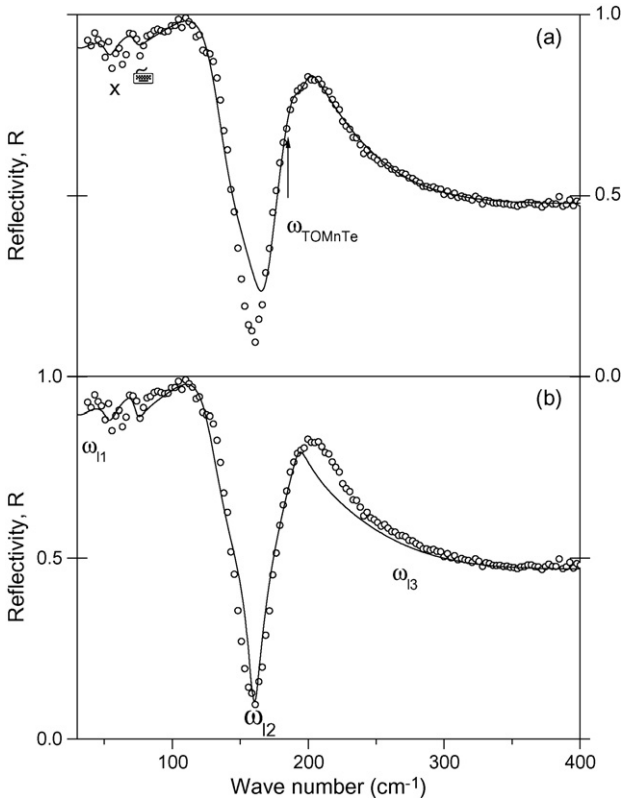

Fig. 2. Far-infrared reflection spectrum of the $Pb_{0.98}Mn_{0.02}Te$ at temperature of 80 K. Solid line is calculated spectrum obtained by a fitting procedure based on the model for plasmon–two different phonon coupling (Eq. (2); $m = 1$ and $n = 2$), with two sets of parameters.

The first term in Eq. (11) represents coupling of one plasmon and one LO phonon mode ($\omega_{lj} = \omega_{\pm}, j = 1, 2$), second term represents coupling of one plasmon and two different LO phonon modes ($\omega_{lj}, j = 1, 2, 3$), while the uncoupled mode of the crystals are represented by the third term.

The parameters adjustment was carried out automatically, by means of the least-square fitting of theoretical (R) and experimental (R_e) reflection coefficients at q arbitrarily taken points:

$$\chi = \sqrt{\frac{1}{q}\sum_{j=1}^{q}(R_{ej} - R_j)^2}, \tag{12}$$

where:

$$R = \left|\frac{\sqrt{\varepsilon} - 1}{\sqrt{\varepsilon} + 1}\right|^2 \tag{13}$$

and ε is given by Eq. (11). The value of χ was minimized until it become comparable with the usual experimental error (less than 2%). The cross-sections of multi-dimensional $\chi(\omega_j, \gamma_j)$ surface were calculated, multiplying each parameter alternately by a varying factor $(1 \pm \delta)$ while all the others are fixed on a determined level. Such sections gave evidence of the precision of the analyses. Practically, for all samples the determination errors of the eigenfrequencies and damping coefficients were about 3–6 and 10–15%, respectively.

4. Results and discussion

The far-infrared reflection spectra of $Pb_{1-x}Mn_xTe$ ($x = 0.0002$, 0.002, 0.02 and 0.1) mixed crystals in the temperature range from 80 to 300 K, and spectral range from 40–400 cm^{-1} are shown in Fig. 3. The experimental data are marched by circles. The solid lines were obtained using the dielectric function from Eq. (11).

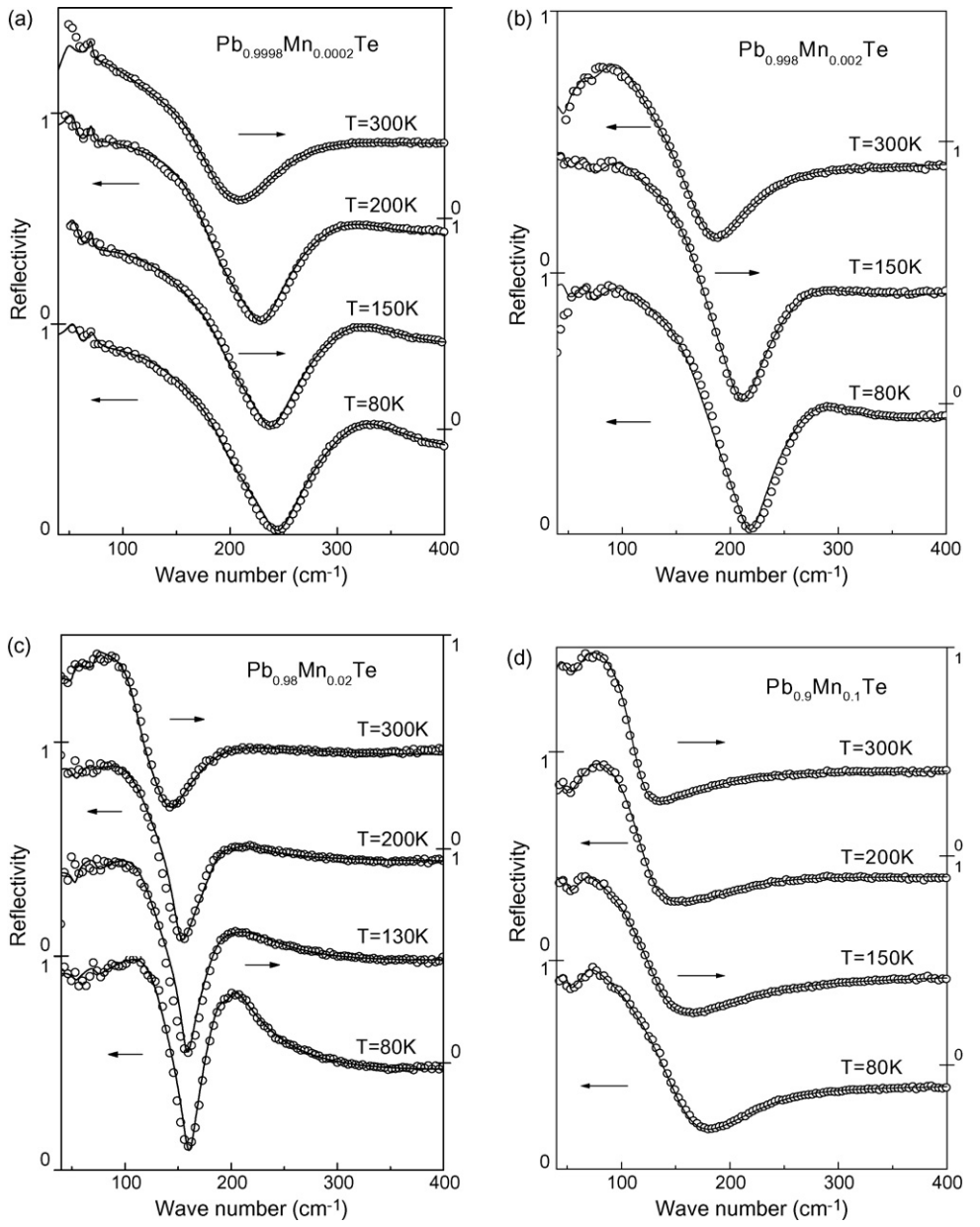

Fig. 3. Far-infrared reflection spectra of mixed crystals $Pb_{0.9998}Mn_{0.0002}Te$ (a), $Pb_{0.998}Mn_{0.002}Te$ (b), $Pb_{0.98}Mn_{0.02}Te$ (c) and $Pb_{0.9}Mn_{0.1}Te$ (d), in the temperature range from 80 to 300 K. Solid line is calculated spectra obtained by the fitting procedure based on the model for plasmon–phonon coupling and plasmon–two different phonon coupling (Eq. (11)).

As a result of the best fit we obtained the frequencies of plasmon–LO phonon coupled modes (ω_+, ω_-) (first term in Eq. (11)), and plasmon–two different LO phonon coupled modes (ω_{l1}, ω_{l2} and ω_{l3}) (second term in Eq. (11)). Values for ω_{LO} and ω_P we calculated from Eq. (4), and values for ω_{LO1} and ω_{LO2} from Eqs. (5)–(10), as it was described in Section 3. The characteristic parameters obtained by described procedure are shown in Fig. 4.

In Fig. 4 we present eigenfrequencies of the plasmon–two different LO phonon coupled modes (a) and plasmon–phonon coupled modes (b) for different compositions and different temperatures. The solid lines are obtained using Eq. (3) in the case of the plasmon–phonon coupled modes (b) and Eq. (5) for plasmon–two different phonon coupled modes (a). The solid circles (●) refer to eigenfrequency spectra $\omega_\pm$ (plasmon–phonon coupling) and ω_{lj} ($j = 1, 2, 3$) (plasmon–two different phonon coupling) obtained by Eq. (11). The agreements between calculated plasmon–LO

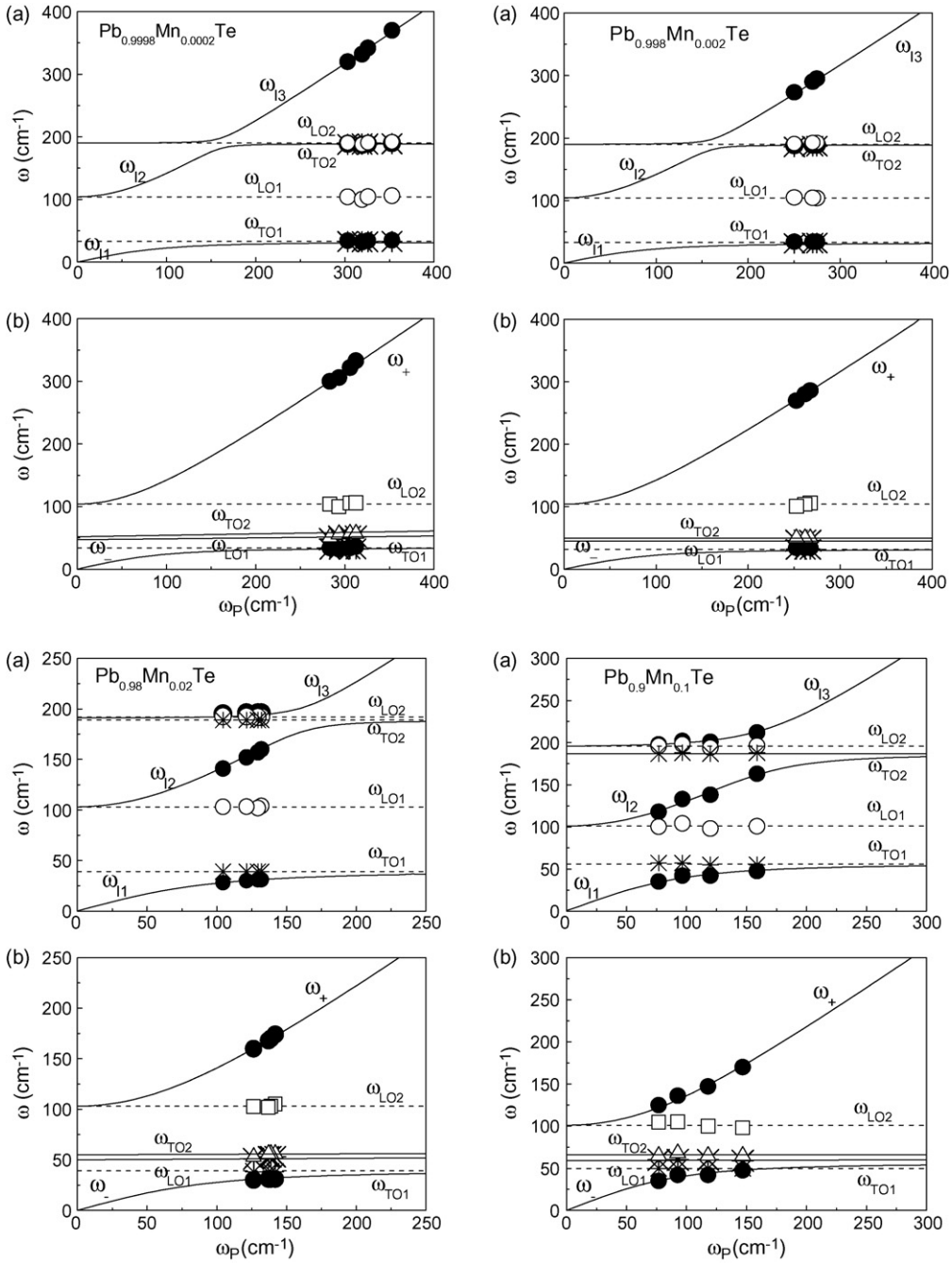

Fig. 4. The eigenfrequencies of mixed crystals $Pb_{0.9998}Mn_{0.0002}Te$, $Pb_{0.998}Mn_{0.002}Te$, $Pb_{0.98}Mn_{0.02}Te$ and $Pb_{0.9}Mn_{0.1}Te$: (a) plasmon–two different LO phonon modes (solid lines, Eq. (5)) and (b) plasmon–LO phonon modes (solid lines, Eq. (3)). (●) eigenfrequency spectra $\omega_{\pm}$ (plasmon–phonon coupling) and ω_{lj} ($j = 1, 2, 3$) (plasmon–two different phonon coupling) obtained by Eq. (11); (○) calculated values for ω_{LO1} and ω_{LO2} (Eq. (10)), (□) calculated values for ω_{LO2} (Eq. (4)); (△) ω_{LO1} (Eq. (11)), (*) ω_{TO1} and ω_{TO2} (Eq. (11)).

phonon mode and plasmon–two different LO phonon mode frequencies, with experimental values, obtained as a best fit from Eq. (11), are very good. Values corresponding ω_{TO1} and ω_{TO2} (Eq. (11)) are given by stars (*). The open circles in Fig. 4 a represent the calculated values for ω_{LO1} and ω_{LO2} (Eq. (10)), open squares (□) represent calculated values for ω_{LO2} (Eq. (4)) and by open triangles (Δ) are denoted values for ω_{LO1} (Eq. (11)). The experimental data analysis showed that plasma frequency (ω_P) increases with the temperature decrease.

Table 1
Parameters in the model for $Pb_{1-x}Mn_xTe$

	a (10^{-10} m)	ω_{TO} (cm^{-1})	ω_{LO} (cm^{-1})	ε_0	ε_∞
PbTe	6.462	46	114	400	65.13
MnTe (cubic structure)	6.341	185	216	11	8.07
MnTe (orthorombic structure)	4.106	126	184	9.67	7.28

This unusual situation can be explained in the following way: coexistence of the plasmon–LO phonon and the plasmon–two different LO phonon coupling in $Pb_{1-x}Mn_xTe$ alloy is induced by the fact that MnTe could have orthorhombic type crystal structure, as well as cubic type of structure [15]. Therefore, if MnTe has orthorhombic type of structure, plasmon–LO phonon coupling arise, while in the case when MnTe has cubic crystal structure plasmon–two different LO phonon coupling takes place, which will be confirmed later.

In order to describe phonon properties of the $Pb_{1-x}Mn_xTe$ mixed crystal, we apply a model for phonon mode behaviour for the ternary compound $A_{1-x}B_xC$ based on the model of Genzel et al. [26], and then check the agreement between theoretical and experimental results. The basic assumptions of applied model are that A and B cations are randomly distributed in the cation sublattice and vibrate with the same phase and amplitude. We take into account local electric field (E_{loc}) and connect microscopic and macroscopic parameters using Born–Huang procedure [27]. Also, we neglect the dependence of the force constant between first neighbours on concentration (x), but we involve the second-neighbour to describe phonon properties of $Pb_{1-x}Mn_xTe$ alloy. Macroscopic parameters are given in Table 1 [28].

The force constants between the second neighbours were determined from impurity modes. As we already said MnTe could have stable orthorhombic NiAs type of crystal structure, as well as stable high-temperature cubic NaCl type structure [29]. Depending on structure impurity modes appear at ~52 cm^{-1} (NiAs structure) and at ~190 cm^{-1} (NaCl structure). In principle, when the semiconductor is doped with a substitutional impurity [21] (in our case

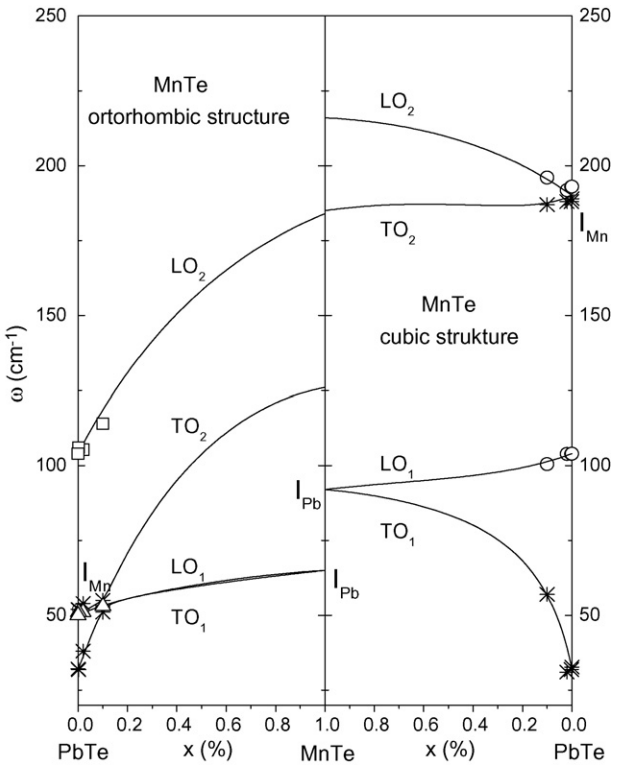

Fig. 5. Concentration dependence of the optical mode frequencies of $Pb_{1-x}Mn_xTe$ mixed crystal. (○) Calculated values for ω_{LO1} and ω_{LO2} (Eq. (10)), (□) calculated values for ω_{LO2} (Eq. (4)); (△) ω_{LO1} (Eq. (11)), (*) ω_{TO1} and ω_{TO2} (Eq. (11)).

manganese), and if the substitution takes place with the atoms of higher mass (in this case Pb), a lighter impurity leads to two modes: localized mode which rises out of the top of the optical band, and gap mode which is situated above the acoustic and below optical band of the host lattice. Therefore, manganese gives two impurity modes, at ~52 and ~190 cm^{-1}. These mode positions are estimated as the best fit from Fig. 5, on the basis of the represented model. The position of Pb impurity in orthorombic structure MnTe was estimated in the simplest way, which was described in detail in [30]:

$$\omega_{I(\mathrm{Pb})} = \omega_{\mathrm{TO}}(\mathrm{MnTe_{NiAs}})\sqrt{\frac{M_{\mathrm{Mn}}}{M_{\mathrm{Pb}}}} \approx 96.1\,\mathrm{cm}^{-1} \tag{14}$$

Pb impurity mode in cubic structure MnTe is determined at the same way

$$\omega_{I(\mathrm{Pb})} = \omega_{\mathrm{TO}}(\mathrm{MnTe_{NaCl}})\sqrt{\frac{M_{\mathrm{Mn}}}{M_{\mathrm{Pb}}}} \approx 64.7\,\mathrm{cm}^{-1} \tag{15}$$

The optical phonon modes behaviour is presented in Fig. 5. The solid lines were obtained by described model. Experimental values are marked by the same marks as in Fig. 4.

If the solid solutions $Pb_{1-x}Mn_xTe$ are formed of manganese-telluride cubic structure (NaCl type of structure) due to the sameness of the crystal structure, impurity mode is formed at ~190 cm^{-1}, and therefore the two-mode behaviour of phonons arose (each TO–LO mode pair for the end members degenerates to an impurity mode). In this case two independent optical ranges (bonds) are formed and each of the LO phonons (LO_1 and LO_2) interact with plasma, as it shown in Fig. 4a. In the second case, manganese telluride has orthorhombic structure (NiAs type of structure) the impurity mode will be formed at about 52 cm^{-1}, so the phonons will show, in this case, intermedial one–two mode (LO-mode frequency shifts continuously from PbTe to MnTe, while the others mode resemble two-mode case). In the mentioned case one optical range (band) is formed, hence only ω_{LO2} phonon interacts with plasma.

Therefore, in this solid solution exists intermedial and two mode behaviour of long wavelength optical phonons, depending on the local structure of MnTe.

5. Conclusion

As a method to investigating phonon properties of $Pb_{1-x}Mn_xTe$ mixed crystal we used far-infrared spectroscopy. We find out that in this system the plasmon–phonon and plasmon–two different phonon coupling occur at the same time. Also, we identify that the long wavelength optical phonon modes of these mixed crystals showed an intermediate and two-mode behaviour. In the case when MnTe has orthorhombic (NiAs) local crystal structure we reveal that the plasmon–LO phonon coupling occur; in that case long wavelength optical phonons exhibit intermedial type of behaviour. When MnTe has local cubic type of structure we find out that plasmon–two different LO phonon coupling taking place, as well as two-mode optical phonon behaviour.

Acknowledgement

This work is supported by Serbian Ministry of Science and Environmental Protection under Project 141028B.

References

[1] M.E. Lines, A.M. Glass, Principles and Applications of Ferroelectrics and Related Materials, The Int. Series of Monographs on Physics, Clarendon, Oxford, 1977.
[2] H. Kawamura, in: W. Zawadski (Ed.), Narrow-Gap Semiconductors, Physics and Applications, Lecture Notes in Physics,, vol. 33, Springer, Berlin, Heidelberg, New York, 1980.
[3] B.A. Volkov, L.I. Ryabova, D.R. Khokhlov, Uspekhi Fizicheskih Nauk, Russian Academy of Science 172 (8) (2002) 875 [Physics–Uspekhi 45 (8) (2002) 819].
[4] T. Shimada, Kh.I. Kobayasi, Y. Katayama, K.F. Komatsubara, Phys. Rev. Lett. 39 (1977) 143.
[5] W. Jantsch, A. Lopez-Ortego, G. Bauer, Infrared Phys. 18 (1978) 877.
[6] D.G. Adrianov, C.A. Belokon, C.O. Klimonskii, V.M. Lakeenkov, Fiz. Tekh. Poluprovodn. 22 (1988) 670.
[7] J. Niewodniczanska-Zawadzka, G. Elsinger, L. Pametshofer, Physica B and C C117 (1983) 458.
[8] A.V. Brodovoi, G.V. Lashkarev, M.B. Radchenko, E.I. Sl'inko, K.D. Tovstuk, Fiz. Tekh. Poluprovodn. 18 (1984) 1547 [Sov. Phys. Semicond. 18 (1984) 970].

[9] J. Nuerwirth, W. Jantsch, L. Palmetchhofer, W. Zulehner, J. Phys. C 19 (1986) 2475.
[10] Z. Korczak, M. Subotowicz, Phys. Stat. Sol. (a) 77 (1983) 497.
[11] J.J. Banewicz, R.F. Heidelberg, A.H. Luxem, J. Phys. Chem. 65 (1961) 615.
[12] N. Kunitami, Y. Hamagauchi, S. Anzai, J. Phys. 25 (1964) 568.
[13] H. Yadaka, T. Harada, E. Hirahara, J. Phys. Soc. Jpn. 17 (1961) 875.
[14] E. Uchida, H. Kondoh, N. Fukuoka, J. Phys. Soc. Jpn. 11 (1956) 27.
[15] F. Hulliger, Struct. Bond. 4 (1968) 190.
[16] A. Golubović, S. Nikolić, J. Trajić, S. Đurić, N. Romčević, M. Romčević, A.J. Nadolny, B. Taliashvili, V. Domukhovski, V.N. Nikiforov, Mater. Sci. Forum 453 (2004) 99.
[17] N. Romčević, A. Golubović, M. Romčević, J. Trajić, S. Nikolić, S. Đurić, V.N. Nikiforov, J. Alloys Compd. 402 (2005) 36.
[18] J. Trajić, M. Romčević, N. Romčević, S. Nikolić, A. Golubović, S. Đurić, V.N. Nikiforov, J. Alloys Compd. 365 (2004) 89.
[19] JCPDS card number 18-0813, 2007.
[20] JCPDS 40-1195, 2007.
[21] E. Burstein, A. Pinczuk, R.F. Wallis, in: D.L. Carter, R.T. Bate (Eds.), The Physics of Semimetals and Narrow-Gap Semiconductors, Pergamon, New York, 1971, p. 251.
[22] M.A. Kinch, D.D. Buss, Solid State Commun. 11 (1972) 319.
[23] V. Gopal, Infrared Phys. 18 (1978) 121.
[24] S. Takaoka, T. Hamaguchi, S. Shimomura, K. Murase, Solid State Commun. 54 (1985) 99.
[25] A.A. Kuharskii, Solid State Commun. 8 (1970) 1275.
[26] L. Genzel, T.P. Martin, C.H. Henry, Phys. Stat. Sol. (b) 62 (1974) 83.
[27] M. Born, K. Huang, Dynamical Theory of Crystal Lattices, Clarendon Press, Oxford, 1954.
[28] J. Niewodniczanska-Zawadzka, A. Szczerbakov, Solid State Commun. 34 (1980) 887.
[29] N. Gonzales-Szwacki, E. Przezdziecka, E. Dynowska, P. Boguslawski, XXXIII International School on the Physics of Semiconducting Compounds, ThP15 105 Jaszowiec, 2004.
[30] S. Venigopalan, A. Petrov, R.R. Galazka, A.K. Ramdas, S. Rodriguez, Phys. Rev. B 25 (1982) 2681.